A New Fast Algorithm to Completely Account for Non-Lambertian Surface Reflection of the Earth

Wenhan Qin
Raytheon, ITSS Corporation, Lanham, Maryland

Jay R. Herman
Atmospheric Chemistry and Dynamics Branch, NASA Goddard Space Flight Center, Maryland

Ziauddin Ahmad
Systems and Applied Sciences Corporation, Riverdele, Maryland

Abstract. Surface BRDF influences not only radiance just above the surface, but that emerging from the top of the atmosphere (TOA). In this study we propose a new, fast and accurate, algorithm CASBIR (correction for anisotropic surface bidirectional reflection) to account for such influences on radiance measured above TOA. This new algorithm is based on 4-stream theory that separates the radiation field into direct and diffuse components in both upwelling and downwelling directions. This is important because the direct component accounts for a substantial portion of incident radiation under a clear sky, and the BRDF effect is strongest in the reflection of the direct radiation reaching the surface. The model is validated by comparison with a full-scale, vector radiation transfer model for the atmosphere-surface system (Ahmad and Fraser, 1982). The result demonstrates that CASBIR performs very well (with overall relative difference of less than 1%) for all solar and viewing zenith and azimuth angles considered in wavelengths from UV to near-IR over 3 typical, but very different surface types. Application of this algorithm includes both accounting for non-Lambertian surface scattering on the emergent radiation above TOA and a potential approach for surface BRDF retrieval from satellite measured radiance.

1. Introduction

The radiance observed by satellites at the top of the atmosphere is the backscattered portion of incident solar radiation by the Earth's ground-atmosphere system. This radiance can be separated into two components: one from purely atmosphere backscattering (path reflection), and the other from the radiance reflected by the underlying surface and transmitted through the atmosphere toward the satellite or in-atmosphere instrument. Traditional atmosphere radiative transfer (RT) models usually assume isotropic scattering of the lower boundary (Lambertian surface) when calculating the contribution from the underlying surface (see Dave, 1964, for example).

However, natural surfaces are usually non-Lambertian, i.e., they scatter light anisotropically. They all exhibit some degree of bidirectional reflection properties. The most common are specular reflection that occurs for forward scattering when incident angle is equal to reflection angle (e.g., sunglint for water surfaces), and hotspot phenomenon where the strongest backscattering occurs when the source light is exactly

behind the viewer for porous media such as vegetated surfaces (Qin and Goel, 1995). The change in surface reflectances with both solar and viewing directions is often referred to as the surface BRDF (bidirectional reflectance distribution function) property. This property has been considered and investigated by simulation of radiation propagation in porous media and surface reflectance modeling for vegetation covers for decades (see Goel, 1988; Qin and Liang, 2000).

Surface BRDF affects the emergent radiation from the top of the atmosphere as well as radiation just above the surface. Early studies for both a Rayleigh atmosphere (Coulson et al., 1966) and a turbid atmosphere (Keopke and Kriebel, 1978) found significant differences in radiance at TOA over natural surfaces and their Lambert-model equivalents even though their albedos were equal. Fitch (1981) did a similar study for three types of natural soil surfaces based on laboratory measurements of surface bidirectional reflectance combined with an atmosphere-surface model. He considered polarization and multiple scattering between the two media (the atmosphere and the underlying surface) up to five orders of scattering in the vector radiative transfer model. Ahmad and Fraser (1982) developed a full-scale, vector RT model for the atmosphere-ocean system, in which the anisotropy of scattering from a rough ocean is incorporated.

To consider interactions between the atmosphere and the underlying non-Lambertian surface, Tanre et al. (1983) specified the radiation emerging from the top of the atmosphere (TOA) in five parts: incident direct/diffuse radiation, directly/diffusely transmitted through the atmosphere after surface reflection, plus a term for multiple scattering between the surface and the atmosphere. In their final formulation, however, the multiple-scattering contribution is ignored. The 6S model [Vermote et al., 1997] added a term to the above formulation trying to approximate multiple scattering contributions. It was not introduced in a physically consistent manner (the authors called the arbitrary addition an approximate term in the paper) because there were no physically-based derivations to justify this addition. Further, the direct-to-diffuse (or diffuse-to-directional) conversion of radiation caused by surface reflection was improperly simulated. In the DISORT code, Stamnes et al. (1988) assumed the surface BRDF to be a function only of the phase angle, so that Legendre polynomials can be used to represent non-Lambertian surface reflection. Since it only represents a single angle, this assumption is not valid in general. Even for a single angle, the ability of Legendre functions to represent the surface BRDF is quite limited.

To remove formulation uncertainties in the application of such algorithms as applied to general situations, it is desirable to base the derivation on a consistent consideration of the physics. The new algorithm presented below will improve accuracy when accounting for the surface BRDF, as well as providing fast computational implementation. Comparisons with a full radiative transfer treatment of the BRDF effect (using a modified version of the Guass-Seidel approach based on Ahmad and Fraser, 1982) validate the algorithm's accuracy and show the need for computational speed in a highly accurate approximation.

Radiation incident on a surface is partially specular (collimated) and partially diffuse. The specular component results from transmission of the direct solar beam through the atmosphere, while the diffuse component results from atmosphere scattering of the incident solar beam and downward scattering of upwelling radiation after reflection from the surface. The BRDF effect is strongest in the reflection of the specular component, which can be more than 80% of total incident solar radiation (in visible and near-infrared regions) under a clear sky. In order to capture this BRDF effect, the direct (or collimated) component has to be treated separately from the diffuse component when modeling its interaction with the surface. Also, to completely take account of surface BRDF effects on measurements above TOA, one has to consider the conversion between direct or directional radiation and diffuse radiation from surface reflection, as well as multiple scattering between the atmosphere and the surface. These goals can be achieved by applying well-known four-stream theory (Hapke, 1981; Li et al., 1996; Qin and Liang, 2000) to simulate radiation interaction in the boundary between two media.

In this study, we will express radiation flux in terms of diffuse (in upwelling and downwelling directions) and direct or directional (collimated in a specified direction) components. This division will ensure that a correct surface reflection coefficient is applied for a given set of incoming and outgoing radiation from surface reflection (see section 2.2.1 for details). When dealing with multiple scattering between two media, the conversion and multiple interactions among all types of radiation (downwelling and upwelling direct and diffuse) are fully taken into account with proper reflection coefficients applied, including all orders of multiple scattering. Within the limitations of a 4-stream approximation, this will overcome most of the weaknesses in previous atmosphere-surface models incorporating surface BRDF characteristics in the lower boundary. The new algorithm will produce the most complete high-speed approximation of multiple scattering between the surface and the atmosphere to date.

In the following section, we will describe the development of this new algorithm: Correction for Anisotropic Surface BIdirectional Reflection (CASBIR), including determination of the various coefficients. Then, we will compare the results with that from a precise, vector-based atmospheric radiative transfer (RT) model for a pure Raleigh atmosphere [Ahmad and Fraser, 1982]. Some concluding remarks and application issues will be discussed in the last two sections.

2. Algorithm Development

For a Lambertian surface with surface reflectance r_s, the reflectance above the atmosphere can be expressed as follows

$$R_a(v) = r_0 + \frac{T_\downarrow(i) \cdot r_s \cdot T^\uparrow(v)}{1 - S_b \cdot r_s}, \tag{1}$$

where i, v are illumination (solar) and viewing directions. r_0 is the path scattering-reflectance of the atmosphere. $T_\downarrow$ is the total transmittance from the top of the atmosphere to the ground along the path of the incoming solar beam, and $T^\uparrow$ is the total transmittance from the ground to the top of the atmosphere in the view direction of the satellite. S_b is

the fraction of the upward diffuse flux backscattered from the atmosphere to the Earth's surface. For a non-Lambertian surface, surface reflectance changes with both illumination and viewing directions. This, combined with the anisotropic diffuse irradiance incident upon the surface, means Eq.(1) could result in considerable errors in radiance calculations. A new algorithm to account for non-Lambertian surface reflection is derived below.

Consider an atmosphere bounded below by a non-Lambertian reflecting surface with bidirectional reflectance $r(i, v)$. We divide the radiation field in the medium into two components (fluxes): diffuse (E) and direct (or directional) (F). Symbols "↑" and "↓" stand for upwelling and downwelling components with superscript (or subscript) for quantities at the upper (or lower) boundary of the atmosphere (see Fig.1). We also define σ as the path reflectance, t as the path transmittance, and r as the boundary reflectance. Each coefficient has two subscript symbols, "*d*" (direct or directional) or "*h*" [diffuse or hemispheric (i.e., the average over the hemisphere)], to indicate photon status before and after interaction. Therefore, there are four combinations of these two symbols: "*dd*", "*dh*", "*hd*" and "*hh*" with the first symbol indicating the initial status of photons (incoming) and the second one for the resulting photon status after interaction (outgoing). For example, subscript "*dh*" indicates the incoming photons from a specific direction being diffusely scattered into the whole hemisphere, either by backward atmospheric path scattering (reflection) (as in σ_{dh}) or forward path scattering (transmission) (as in t_{dh}) or boundary reflection (as in r_{dh}).

As shown in Fig.1, at the top of the atmosphere, the only incident radiation flux, $F^{\downarrow}(i)$, is the direct solar beam with zenith angle θ_i and azimuth angle φ_i. The radiation scattered into the sensor's field of view (FOV) in the view direction (θ_v, φ_v), $F^{\uparrow}(v)$, is the sum of three components:

$$F^{\uparrow}(v) = \sigma_{dd}(i,v)\cdot F^{\downarrow}(i) + t_{dd}(v)\cdot F_{\uparrow}(v) + t_{hd}(v)\cdot E_{\uparrow}, \qquad \textbf{(2)}$$

where $F_{\uparrow}(v)$ is the radiation flux in direction v, and $E_{\uparrow}$ is the upwelling diffuse flux leaving the surface. σ_{dd} is the purely atmospheric backscattering coefficient [also called path reflectance, equal to r_0 in Eq.(1)], t_{dd} is the direct part of $T^{\uparrow}$, i.e., atmospheric transmittance for collimated radiation in the satellite viewing direction, and t_{hd} is the diffuse part of $T^{\uparrow}$, i.e., the efficiency of atmospheric scattering of upward diffuse radiation coming from the surface toward the satellite in the viewing direction (θ_v, φ_v) at TOA. We will discuss these and other coefficients in details in Section 2.2.

2.1. Calculation of $F_{\uparrow}(v)$ and $E_{\uparrow}$

Based on the above definitions, the equations to compute $F_{\uparrow}$ and $E_{\uparrow}$ can be expressed as

$$\begin{aligned} F_{\uparrow}(v) &= r_{dd}(i,v)\cdot F_{\downarrow}(i) + r_{hd}(v)\cdot E_{\downarrow} \\ E_{\uparrow} &= r_{dh}(i)\cdot F_{\downarrow}(i) + r_{hh}\cdot E_{\downarrow}. \end{aligned} \qquad \textbf{(3a)}$$

The above equations consider the conversion between directional and diffuse radiation caused by surface reflection. The solution of the above equation set can be obtained by first evaluating the 1st-order scattering components of $E_{\downarrow}$ and $E_{\uparrow}$, then the 2nd-order components, the 3rd-order components, and so on. By considering multiple bounces of

photons between two layers/media, Li et al. (1996) deduced a set of closed form expressions including all orders of multiple bounces for the above quantities. Based on our definitions, the solution to the above equations for the lower boundary of the atmosphere-surface system can be written as follows:

$$F_{\uparrow}(v) = r_{dd}(i,v)\cdot F_{\downarrow}(i) + r_{hd}(v)\cdot\left[t_{dh}(i)\cdot F^{\downarrow}(i) + \sigma_{hh}\cdot E_{\uparrow}\right]$$
$$E_{\uparrow} = \frac{r_{dh}(i)\cdot F_{\downarrow}(i) + r_{hh}\cdot\left[t_{dh}(i)\cdot F^{\downarrow}(i)\right]}{1 - r_{hh}\cdot\sigma_{hh}} \qquad \textbf{(3b)}$$
$$F_{\downarrow}(i) = t_{dd}(i)\cdot F^{\downarrow}(i).$$

After replacing $F_{\uparrow}$ and $E_{\uparrow}$ in Eq.(2) with the above expressions in 3a and 3b, and making some mathematical manipulations, we finally get the reflectance at TOA -- R_a, defined as the ratio of $F^{\uparrow}(v)/F^{\downarrow}(i)$, in a form of matrix, as

$$R_a(i,v) = \sigma_{dd}(i,v) + \frac{\mathbf{T}(i)\cdot\mathbf{R}(i,v)\cdot\mathbf{T}(v) - t_{dd}(i)\cdot t_{dd}(v)\cdot|\mathbf{R}(i,v)|\cdot\sigma_{hh}}{1 - r_{hh}\cdot\sigma_{hh}}, \qquad \textbf{(4a)}$$

where matrices $\mathbf{T}(i)$, $\mathbf{T}(v)$ and $\mathbf{R}$ are defined as

$$\mathbf{T}(i) = \left[t_{dd}(i) \quad t_{dh}(i)\right],\ \mathbf{T}(v) = \begin{bmatrix} t_{dd}(v) \\ t_{hd}(v)\end{bmatrix},\ \mathbf{R}(i,v) = \begin{bmatrix} r_{dd}(i,v) & r_{dh}(i) \\ r_{hd}(v) & r_{hh}\end{bmatrix}. \qquad \textbf{(4b)}$$

One can see Eq.(4a) is similar to Eq.(1) in form, with

$$T_{\downarrow}(i)=t_{dd}(i)+t_{dh}(i),\ T^{\uparrow}(v)=t_{dd}(v)+t_{hd}(v),\ \text{and}$$
$$r_0=\sigma_{dd},\ S_b=\sigma_{hh},\ r_s=r_{hh}. \qquad \textbf{(4c)}$$

For non-Lambertian surfaces, single variables such as $T^{\uparrow}$, $T_{\downarrow}$ and r_s in Eq.(1) are replaced by the corresponding matrices. Also, there is an extra term in Eq.(4a), which is a function of the determinant $|\mathbf{R}|$, calculated as

$$|\mathbf{R}|=r_{dd}\cdot r_{hh}-r_{dh}\cdot r_{hd}. \qquad \textbf{(4d)}$$

Since $|\mathbf{R}|$ could be positive or negative, depending on solar and viewing directions, and the degree of non-Lambertian reflection from the surface, the contribution from non-Lambertian surface reflection could be more or less than that from its Lambert equivalent. For a Lambertian surface, Eq.(4a) reduces to Eq.(1), because the four components in $\mathbf{R}$ are equal to r_{hh}, so that $|\mathbf{R}|=0$.

2.2. Estimation of various coefficients

There are two types of coefficients involved in CASBIR [Eq.(4a)]: atmosphere related [$\mathbf{T}(i)$, $\mathbf{T}(v)$, each has two components, and σ, which has four components, but only two (σ_{dd}, σ_{hh}) are used here] and surface related ($\mathbf{R}$, which has four components). Fortunately, as shown below, coefficients in one group are independent of those in the other group, and can be determined separately. For example, atmospheric-property

related coefficients could be calculated by using any atmospheric RT model based on a Lambertian surface assumption. Similarly, components of **R** can be determined from surface bidirectional reflectance distributions, regardless of atmospheric conditions, because surface BRDF is an intrinsic property of the surface, independent of atmospheric conditions. In the following, we will describe determination of coefficients in both groups.

2.2.1. Boundary reflectance coefficients

Surface BRDF is the physical quantity to characterize surface reflection. It is determined by surface structures and optical properties (material reflectivity and transmittance), and varies with illumination and observation directions. However, BRDF is defined for an infinitesimal solid angle; it can be modeled, but virtually cannot be measured. In practice, it is often replaced by a measurable alternative -- BRF (bidirectional reflectance factor), quantified as the ratio between radiance reflected from a real surface and that from a perfect Lambertian reflector, assuming all other conditions are the same.

All components of **R** are functions of surface BRF and can be calculated straightforwardly once the surface BRF is determined. In the following, we will discuss the definition and determinations of components of **R**. We leave the discussion on practical methods to determine surface BRF to Section 4.

r_{dd} – bidirectional reflectance r_{dd} can be defined in terms of the BRF, $r(i,v)$,

where
$$r_{dd}(i,v) = r(i,v), \tag{5a}$$

$$r(i,v) = \pi I_{\uparrow}(i,v)/\mu_i F_{\downarrow}(i) \tag{5b}$$

is the surface BRF under direct solar beam (without any skylight). $F_{\downarrow}(i)$ is the direct solar flux incident upon the surface [see Eq.(3b)] in direction i with $\mu_i = \cos(\theta_i)$, and $I_{\uparrow}(i,v)$ is the reflected radiance of $F_{\downarrow}(i)$ from the surface in direction v. As indicated in section 4, $r(i,v)$ can be determined by modeling or measurements for a given surface type.

r_{dh} – directional-hemispheric reflectance r_{dh} specifies the fraction of direct radiation incident upon a surface that is diffusely reflected toward the upper hemisphere ($2\pi^+$). Mathematically it is defined as

$$r_{dh} = \frac{\int_{2\pi^+} I_{\uparrow}(i,\xi)\mu_\xi d\Omega_\xi}{\mu_i F_{\downarrow}(i)}, \tag{6a}$$

where ξ is the scattering direction. Replacing $I_{\uparrow}(i,v)$ with $r(i,v)$ in Eq.(5b) yields

$$r_{dh} = r_h(i), \quad r_h(i) = \frac{1}{\pi}\int_0^{2\pi} d\varphi_\xi \int_0^1 r(i,\xi)\mu_\xi d\mu_\xi. \tag{6b}$$

$r_h(i)$ is the hemispheric reflectance for a specific solar direction.

r_{hd} – hemispheric-directional reflectance r_{hd} is defined as the fraction of downwelling diffuse radiation reflected toward the specific direction v by the surface, i.e.,

$$r_{hd}(v) = \frac{\int_{2\pi^-} L_\uparrow(\zeta, v)\mu_\zeta d\Omega_\zeta}{E_\downarrow}, \tag{7a}$$

where $2\pi^-$ represents the lower hemisphere, ζ is the incident direction of diffuse light upon the surface, and $L_\uparrow$ is the upward reflected radiance of $E_\downarrow$, which equals $r(i,v)E_\downarrow/\pi$. Therefore, we finally have

$$r_{hd}(v) = r_h(v), \quad r_h(v) = \frac{1}{\pi}\int_0^{2\pi} d\varphi_\zeta \int_0^1 r(\zeta, v)\mu_\zeta d\mu_\zeta. \tag{7b}$$

$r_h(v)$ is the hemispheric reflectance for a specific viewing direction. If the surface reflection follows the reciprocity law, i.e., $r(i,v) = r(v,i)$, then $r_h(i) = r_h(v)$ and $r_{dh} = r_{hd}$ if $i=v$.

r_{hh} – hemispheric-hemispheric reflectance r_{hh} is also called bi-hemispheric reflectance. By definition, it is the double integral of the scattered diffuse radiation ($L_\uparrow$) over viewing (upper) and illumination (lower) hemispheres divided by the downwelling diffuse radiation. That is,

$$r_{hh} = \frac{\frac{1}{\pi}\int_{2\pi^-}\left\{\int_{2\pi^-} L_\uparrow(\zeta, \xi)\mu_\zeta d\Omega_\zeta\right\}\mu_\xi d\Omega_\xi}{E_\downarrow}, \tag{8a}$$

where ζ, ξ are source light and scattering directions, respectively. Similar to calculate r_{hd}, the above double integration can be simplified and evaluated as

$$r_{hh} = \text{albedo} = \frac{1}{\pi}\int_0^{2\pi} d\varphi_\xi \int_0^1 r_h(\xi)\mu_\xi d\mu_\xi, \tag{8b}$$

where $r_h(\zeta)$ is the same as $r_h(v)$, expressed in Eq.(7b). Therefore, r_{hh} is the spherical albedo that considers all viewing and illumination directions.

2.2.2. Atmospheric scattering and transmission coefficients

Atmospheric path scattering (σ) and transmission (**T**) coefficients are functions of the atmospheric optical depth (τ_a), single scattering albedo (ω), and phase function (P) of the scatterers and absorbers in the atmosphere. Only the direct component of **T** [see Eq.(4c)] has an analytical expression as

$$t_{dd}(\mu) \equiv t_{dd}(\mu, \tau_a) = \exp(-\tau_a/\mu), \tag{9}$$

where $\mu=\cos(\theta)$, θ is the zenith angle of the light. To estimate other components of σ and **T**, one has to utilize an atmospheric RT model, because there are no analytical expressions available in general. Most atmospheric RT models can provide these coefficients in a form of either numerical solutions or look-up tables (LUTs) for a variety of sun-view geometries and aerosol loadings (e.g., Dave and Gazdag, 1970). The LUT approach is computationally more efficient, especially for practical use in an algorithm for satellite fields of view in a global data set. It has been used for decades (e.g., Dave et al., 1966). However, under some special conditions (e.g., for a pure Rayleigh atmosphere), one may be able to obtain an analytical approximation for these coefficients

(Vermote and Tanre, 1992). These analytical expressions become closer to exact numerical solutions for wavelengths much larger than the particle size of gaseous constituents, because the multiple scattering contribution becomes very small. Since the scattering coefficient σ_{dd} (path reflectance) and σ_{hh} (backward scattering of the upward diffuse flux from the surface) are the same as r_0 and S_b in Eq.(1), their determination will not be discussed here. In the following, we will only discuss the determination of the diffuse components of atmospheric transmission function **T**.

t_{dh} – *directional-hemispheric path transmttance* r_{dh} defines the fraction of downward diffuse flux generated by atmospheric scattering as direct solar beam passes through the atmosphere. It is also called the atmospheric diffuse transmission function. Mathematically, it can be expressed as follows

$$t_{dh}(i) = \frac{\int_{2\pi^-} L_{\downarrow}(i,\xi)\mu_{\xi} d\Omega_{\xi}}{\mu_i F^{\downarrow}(i)}, \tag{10}$$

where $L_{\downarrow}$ is the downwelling diffuse radiance reaching the surface due to atmospheric scattering of the incident direct solar radiation from direction i into direction ξ. Generally, there is no analytical expressions for $L_{\downarrow}$ because of the multiple scattering in the atmosphere. However, numerical results for $L_{\downarrow}$ are available for a given atmosphere type from conventional atmospheric RT models. Therefore, t_{dh} is usually provided for given solar zenith angles and atmospheric conditions (e.g., a given set of τ_a, ω and P).

t_{hd} – *hemispheric-directional path transmttance* t_{hd} is defined as the fraction of upward diffuse flux scattered by atmospheric constituents (molecules and aerosols) toward the satellite in direction v. Similar to t_{dh}, t_{hd} can be estimated from

$$t_{hd}(v) = \frac{\int_{2\pi^-} L^{\uparrow}(\zeta,v)\mu_{\zeta} d\Omega_{\zeta}}{E_{\downarrow}}, \tag{11}$$

where $L^{\uparrow}$ is the upwelling diffuse radiance at the top of the atmosphere scattered toward viewing direction v by atmospheric constituents. With the same reasons for $L_{\downarrow}$, $L^{\uparrow}$ can only be numerically computed in most atmospheric RT models, from which t_{hd} can be evaluated.

3. Validation

To validate CASBIR, we compare the modeled reflectance at TOA with calculations from a full-scale vector atmospheric RT model (Ahmad and Fraser, 1982), here called VRT model. The reason for using this atmospheric model as the standard for comparison is because of its ability to directly incorporate arbitrary surface BRF distributions into the model. We also use the VRT model to calculate the atmosphere related parameters (σ and **T**) needed in CASBIR for validation purpose. A Rayleigh atmosphere in five wavelengths (388 nm, 443 nm, 551 nm, 645 nm, and 870 nm, matching 5 of 10 Triana channels) covering UV to near-IR over three diverse types of surface (desert, grassland and forest) are considered in the comparison. The VRT model has been successfully compared with both DISORT and the Dave vector code for Lambertian surfaces.

To obtain surface BRF distributions, an elaborate 3-D scene BRDF model (Qin et al., 1998; Qin and Gerstl, 1998; 2000) is employed to first generate the 3-D structures of a given surface type and then compute the complete BRF distributions. The input optical properties (reflectance and transmittance of vegetation elements and the soil background) and structural parameters are taken from field measurements (Privette et al., 2000; Walter-Shea et al., 1992; Hall et al., 1992). Our choice of modeled surface BRFs with the 3-D scene model rather than using field BRF measurements is based on the high angular resolution of the simulated BRF data. This enables us to complete the comparison over the whole hemisphere without having to do any interpolations for surface BRF.

Specifically, for each surface type in each wavelength, we produced a look-up table for surface BRF over 16 view zenith angles (VZAs, 6° step) and 16 relative azimuth angles (12° step) for each solar zenith angle (SZA), with a total of 16 LUTs generated for 16 SZAs. Figure 2 shows surface BRF distributions for 551 nm at a SZA of 30° for 3 surface types. Note that the desert exhibits the largest contrast in reflectance between forward and backward directions because its rolling-hill structure (which reflects the topography of natural deserts) produces a significant amount of shadowing near the forward scattering directions. Forest scenes have the sharpest hotspot reflection peak because of the highly heterogeneous structure (large gaps exist in the canopy), and the grassland has the least variations in reflectance compared to the above two. Both grassland and forest have flat soil backgrounds.

Based on the LUTs for surface BRF, the VRT model calculates reflectance at TOA for the Rayleigh atmosphere overlying each non-Lambertian ground surface. It also produces other parameters needed for CASBIR, such as path scattering (σ_{dd} and σ_{hh}) and transmission (t_{dh} and t_{hd}) coefficients. Figure 3 plots the corresponding BRFs at TOA for each surface BRF distribution shown in Fig. 2. Comparison between Figure 2 and 3 for all five wavelengths (not shown here) indicates that BRF effects increase with longer wavelengths, because of the smaller atmospheric optical depth and smaller path-scattering contribution.

Comprehensive comparisons of results are presented in Figs 4-6 and Table 1. Figures 4-6 examine the performance of CASBIR in the solar principal plane (view azimuth in 0-180° transect) for the three types of surfaces. We also include the result from the Lambert equivalents for comparison. For each surface type, we plot three wavelengths (388, 551 and 870 nm) under three solar zenith angles (6, 30, and 60°). CASBIR performs very well for all cases, matching the distributions from the VRT model at all points. As a contrast, however, the Lambert equivalent [Eq.(1) with $r_s=r_{hh}$] produces substantial differences (except for the ultraviolet band, such as 388 nm), especially in the hotspot region or in the visible and near-IR.

Table 1 summarizes the mean and maximum relative differences between the VRT model and CASBIR (or its Lambert equivalent) for all solar and viewing directions considered, and for each surface type (a total of 2912 cases after excluding zenith angles larger than 80°). Numbers in table 1 prove that this simple algorithm is very effective in accounting for surface BRDF influences at all angles. The average percentage difference

is below 0.5% in the UV for all surface types, and over vegetation cover for all wavelengths from UV to near-IR. However, the relative difference goes up to 1% for the desert in the visible. The mean percentage difference under Lambertian assumption is much higher, with the highest up to 43% for the desert in the near-IR. Generally, the difference is larger as surface reflectance increases, indicating the enhanced surface BRDF influence. Therefore, the surface effect is wavelength dependent, simply because of 1) changes in surface material reflectivity with wavelength, and 2) the wavelength dependence of atmosphere scattering. The percentage difference also changes with solar zenith angle, increasing as SZA decreases (see Figs. 4-6), because the contribution from atmospheric path scattering decreases with SZA. Finally, for a given surface type at a fixed wavelength, the surface BRDF effect varies with the type of surface formations and topography, since highly heterogeneous surfaces usually have strong anisotropic scattering, and accordingly, strong surface BRDF.

4. Discussion

For visible and near-IR radiances under clear skies, the above studies demonstrate that surface BRDF has a considerable influence on radiation emerging from the top of the atmosphere. However, evaluation of such effects requires accurate or reliable information on spatial distribution of surface bidirectional reflectance. Currently, this information is mostly obtained from two sources: field measurements or BRDF model simulations. Although field measurements can directly provide the ground truth of surface BRF, it is very labor intensive and only available for very limited areas and a few types of land cover. Need for surface BRF at a global scale cannot be met with this method. On the other hand, BRDF models have the capacity to generate BRF distributions globally. But they have their own limitations: inflexible model applicability and difficulties in determining the needed model input parameters.

Most BRDF models (except 3-D models) only work over specific surface types, and their input parameters are not obtainable globally. Therefore, to solve the above problems, the MODIS surface BRDF/albedo retrieval team uses a kernel-driven model (a linear sum of pre-specified terms characterizing different scattering modes) combined with model inversion technique to obtain the input model parameters to reconstruct surface BRDF (Strahler and Muller, 1999). First, it is assumed that the kernel-driven model has a universal applicability for all the surfaces the satellite will observe. Then, satellite measurements are used to retrieve the model parameters so that the BRF distribution can be calculated by running the model with the retrieved parameters.

Even though the kernel driven method seems the only practical choice to make use of satellite data, this approach still faces a few challenges. First, although kernel-driven models are simple and fast, they are not universal, because land surfaces are very diverse; its scattering nature cannot be characterized by a linear sum of two or three simple, predetermined kernels. Therefore, the model may not have the capacity to capture the BRDF of every type of surface the satellite observes (particularly for highly heterogeneous scenes or mixture pixels). Second, the input parameters retrieved from satellite measurements may not be unique, which could lead to the BRDF pattern

reproduced by such models that is different from the true one for the surface viewed in the pixel. Third, the satellite data used for surface BRDF/albedo retrieval have to be atmospherically corrected. The dilemma here is that the algorithm for atmospheric-effect correction could not produce a correct result for non-Lambertian surfaces without first knowing surface BRF distributions. Therefore, further work is still needed in order to use satellite data for reliable surface BRDF retrieval.

Besides accounting for surface effects on radiation emerging from TOA, our new algorithm (CASBIR) can also be used to retrieve surface BRDF from satellite measurements. Theoretically, this can be done by solving the integral equation [Eq.(4a)] with multi-angular satellite measurements for a clear sky or if the atmospheric profile is known. But practically, there is no guarantee that a unique solution exists for surface BRDF from Eq.(4a). For most satellites there are usually not enough angular samples to ensure a reliable retrieval of surface BRDF from satellite measurements in a short period during which surface BRDF does not change much. These constraints make the direct retrieval approach less attractive and useful.

However, some new thoughts about surface BRDF retrieval can be gained from the result of CASBIR. For example, the similarity of angular patterns of reflectance between above-the-surface and above-the-atmosphere in the near-IR (see Fig.7) indicates that the angular distribution pattern of surface BRDF is well retained in satellite observations for near IR wavelengths under a clear sky. Therefore, if we can obtain such patterns from other sources, we can retrieve surface BRDF from just a single-direction satellite observation (e.g., from nadir). Obviously, a dedicated 3-D BRDF model can help to provide such BRDF patterns if reliable global or regional land cover maps are available. We will detail this approach in other papers in the context of using Triana observations combined with measurements from other satellites (such as SeaWiFS, MODIS, MISR, etc.) to estimate surface radiance and energy budget.

5. Conclusions

A new, fast algorithm to account for non-Lambertian surface scattering on radiation emerging from the top of the atmosphere is developed in this study. Rather than treating photons in every direction equally and precisely, as in the VRT model, in its interaction with the surface, we group radiation into direct and diffuse categories and treat both groups separately. The physical basis for this lies in the fact that the BRDF effect is the strongest in the reflection of the direct incident radiation, which comprises a substantial proportion in the incident radiation under a clear sky. The separation allows us to apply four-stream theory to handle the complicated problem of radiation interaction between two media (the atmosphere and underlying surface), and to develop a simple, analytical algorithm to account for surface BRDF effects on satellite measured radiance.

The comparison with an accurate, full-scale vector atmospheric radiation transfer (VRT) model that is capable of directly incorporating arbitrary surface BRDF as its lower boundary condition, demonstrates that the new fast algorithm is very accurate and effective. The relative difference is less than 0.5% meanly in the UV region for all three

surface types (desert, grassland and forests) or in the spectral region from UV to near-IR for vegetation. Only for deserts in the visible, the relative difference goes up to 1% in average due to largest surface reflection.

The surface BRDF effect is wavelength dependent. It decreases with increasing atmospheric optical thickness and surface reflectance. For a clear sky (a Rayleigh atmosphere), the surface influence increases with wavelength due to decreasing atmospheric path scattering and increasing surface reflectance. For example, in the UV region, the contribution of atmospheric molecular scattering dominates, and surface reflectance is very small (less than 3% for a vegetation surface and 7% for desert or bare soil surfaces), thus the surface BRDF effect is marginal and can be neglected. As the wavelength increases, the contribution by atmosphere scattering declines and surface reflectance rises. Therefore, in the near-IR, the contribution from surface reflection dominates and TOA BRF has almost the same shape as the surface BRF (see the Discussion section). This suggests a new approach to retrieve surface BRDF patterns from satellite observations in the near-IR.

References

Ahmad, Z., and Fraser, R.S. (1982), An iterative radiative transfer code for ocean-atmosphere systems, *J. Atmos. Sci.*, 39, 656-665.

Coulson, K.L., Gray, E.L., and Bouricius, G.M.B. (1966), Effect of surface reflection on planetary albedo, *Icarus*, 5, 139-148.

Dave, J.V. (1964), Meaning of successive iteration of the auxiliary equation in the theory of radiative transfer, *Astrophys. J.*, 140, 1292-1303.

Dave, J.V., and Furukawa, P.M. (1966), Scattered radiation in the ozone absorption bands at selected levels of a terrestrial Rayleigh atmosphere, *Meteorol. Monographs*, 7, 1-10.

Dave, J.V., and Gazdag, J. (1970), A modified Fourier transform method for multiple scattering calculations in a plane parallel Mie atmosphere, *Appl. Opt.*, 9, 1457-1466.

Fitch, B.W. (1981), Effects of reflection by natural surfaces on the radiation emerging from the top of the Earth's atmosphere, *J. Atmos. Sci.*, 38, 2717-2729.

Goel, N.S., (1988), Models of vegetation canopy reflectance and their use in estimation of biophysical parameters from reflectance data, *Remote Sens. Rev.* 4, 1-222.

Hapke, B.W. (1981), Bidirectional reflectance spectroscopy. 1. Theory. *J. Geophys. Res.* **86,** 3039-3054.

Hall, F.G., Huemmrich, K.F., Strebel, D.E., Goetz, S.J., Nickeson, J.E. and Woods, K.D. (1992), *Biophysical, morphological, canopy optical property, and productivity data from the superior national Forest*, NASA Technical Memorandum TM-104568.

Koepke, P. and Kriebel, K.T. (1978), Influence of measured reflection properties of vegetated surfaces on atmospheric radiance and its polarization, *Appl. Opt.*, 17, 260-264.

Li, X. et al., (1996), Simulation of path scattering and multiple bounces of photons between two media, *Science in China*, 26, 457-466 (in Chinese).

Privette, J.L., et al. (2000), The prototype validation exercise (PROVE) for EOS land and atmosphere products, *Remote Sens. Environ.*, (in press).

Qin, W., and Goel, N.S. (1995), An evaluation of hotspot models for vegetation canopies, *Remote Sens. Rev.*, 13, 121-159.

Qin, W., and Liang, S., (2000), Plane-parallel canopy radiation transfer modeling: recent advances and future directions, *Remote Sens. Rev.*, (in press).

Qin W., and Gerstl, S.A.W. (1998), 3-D scene modeling and remote sensing applications, *Proc. Progress in Electromagnetics Research Symposium* (PIERS'98), Nantes, France.

Qin W., and Gerstl, S.A.W. (2000), 3-D scene modeling of semi-desert vegetation cover and its radiation regime, *Remote Sens. Environ.*, (in press).

Qin W., Gerstl, S.A.W., and Deering, D. (1998) Examination of relations between NDVI and vegetation properties using simulated MISR data, *Proc. 18th Int. Geosci. Remote Sens. Symp.* pp. 1243-1245, Seattle, USA.

Stamnes, K., Tsay, S-C., Wiscombe, W. and Jayaweera, K. (1988), Numerically stable algorithm for discrete-ordinate-method radiative transfer in multiple scattering and emitting layered media, *Appl. Opt.*, 27, 2502-2509.

Strahler, A.H., and Muller, J.-P. (1999), *MODIS BRDF/albedo product: algorithm theoretical basis document version 5.0*, NASA MODIS Product ID: MOD43.

Tanre, D., Herman, M. and Deschamps, P.Y. (1983), Influence of the atmosphere on space measurements of directional properties, *Appl. Opt.*, 22, 733-741.

Vermote, E.F., Tanre, D., Deuze, J.L., Herman, M. and Morcrette, J.-J. (1997), Second simulation of the satellite signal in the solar spectrum, 6S: and overview, *IEEE Trans. Geosci. Remote Sens.*, GE-35, 675-686.

Vermote, E.F., Tanre, D. (1992), Analytical expressions for radiative properties of planar Rayleigh scattering media, including polarization contributions, *J. Quant. Spectrosc. Radiat. Transfer*, **47**, 305-314.

Walter-Shea, E A. et al., (1992), Biophysical properties affecting vegetative canopy reflectance and absorbed photosynthetically active radiation at the FIFE site, *J. Geophy. Res.*, 97, 18925-18934.

Table 1. The percentage differences of CASBIR and Lambertian model for all solar and viewing directions considered (excluding zenith angles larger than 80°) over three different surface types under a clear sky (Rayleigh atmosphere).

	wavelength	*388*	*443*	*551*	*645*	*870*
Desert	*(nm)*					
CASBIR	mean	0.41	0.87	1.22	1.00	0.43
	maximum	1.00	2.25	4.36	4.58	2.67
Lamb.	mean	2.10	6.73	19.83	29.34	42.71
	maximum	7.36	18.42	69.73	149.50	373.14
Grassland						
CASBIR	mean	0.06	0.12	0.65	0.13	0.42
	maximum	0.27	0.62	2.05	0.71	1.17
Lamb.	mean	0.56	1.84	7.45	8.42	19.15
	maximum	4.52	11.10	32.75	37.90	66.21
Forest						
CASBIR	mean	0.11	0.24	0.24	0.23	0.28
	maximum	0.39	0.75	0.91	0.72	1.47
Lamb.	mean	1.04	3.08	8.37	11.86	13.22
	maximum	9.43	24.18	41.07	54.53	69.31

Figure captions

Figure 1. A sketch graph to illustrate radiation interaction in atmospheric boundaries using the 4-stream scheme (see text for details).

Figure 2. Simulated surface BRFs at solar zenith angle of 30° in 551 nm over (a) desert, (b) grassland and (c) forest. The polar coordinate system represents view zenith angle with 0° (nadir) at the center of the plot and 90° at the edge. The solar azimuth angle increases clockwise with the hot spot direction at 180° and forward scattering direction at 0°.

Figure 3. Same as in Figure 2 but for reflectance at the top of the atmosphere.

Figure 4. Comparison among TOA reflectances over the desert scene from the VRT model (solid line), CASBIR (plus sign) and the Lambertian equivalent (dash line) in the solar principal plane in 388, 551 and 870 nm (top to bottom) at solar zenith angle of 6, 30 and 60° (left to right).

Figure 5. Same as in Figure 4 but over grassland.

Figure 6. Same as in Figure 4 but over forest scene.

Figure 7. Similarity of BRF shapes between above-the-surface and above-the-atmosphere at solar zenith angle of 30° in 870 nm over (a) desert, (b) grassland and (c) forest.

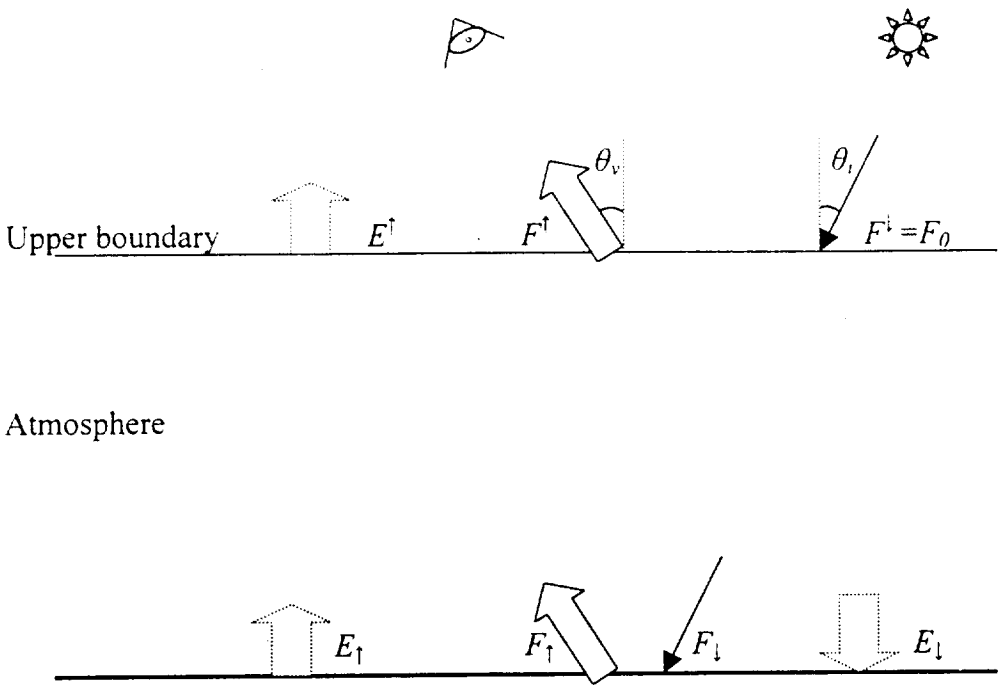

Figure 1. A sketch graph to illustrate radiation interaction in atmospheric boundaries using the 4-stream scheme (see text for details).

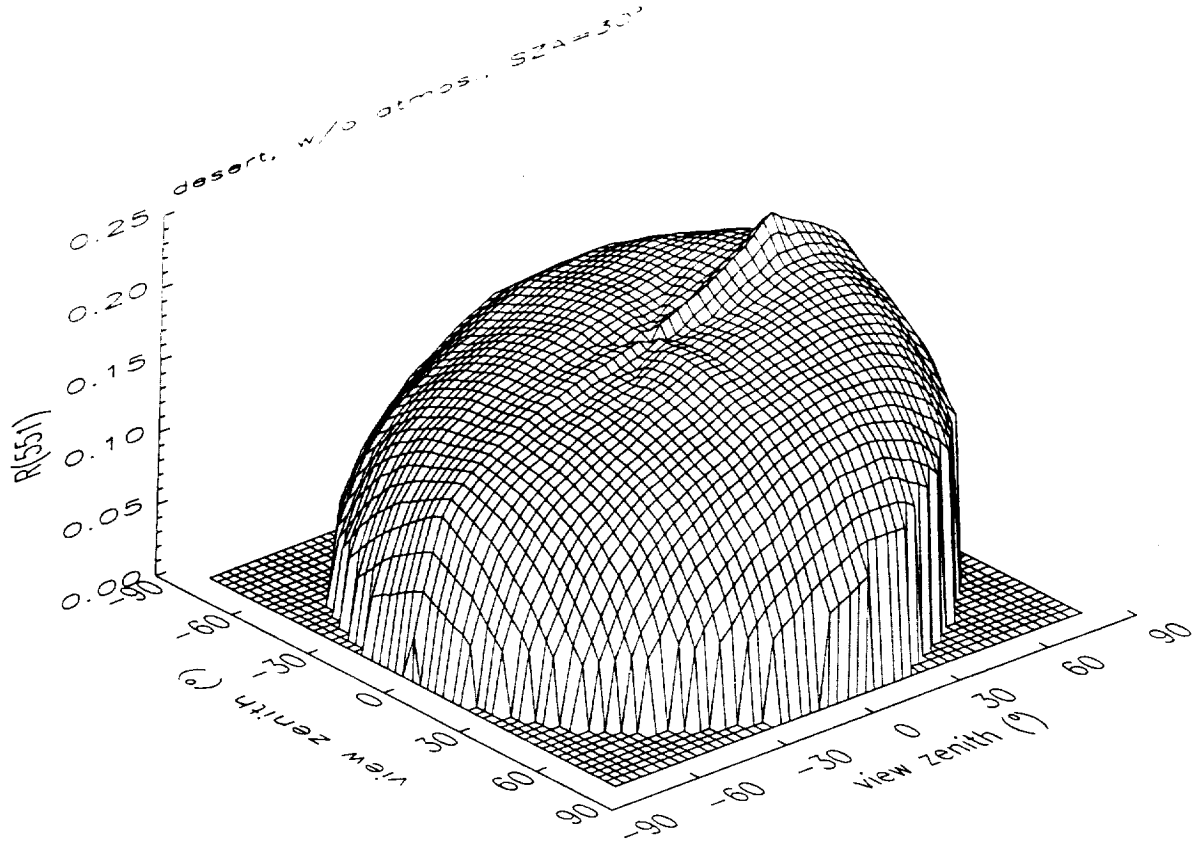
desert, w/o atmos., SZA=30°
R(551)
0.25
0.20
0.15
0.10
0.05
0.00
-90
-60
-30
0
30
60
90
view zenith (°)
-90
-60
-30
0
30
60
90
view zenith (°)

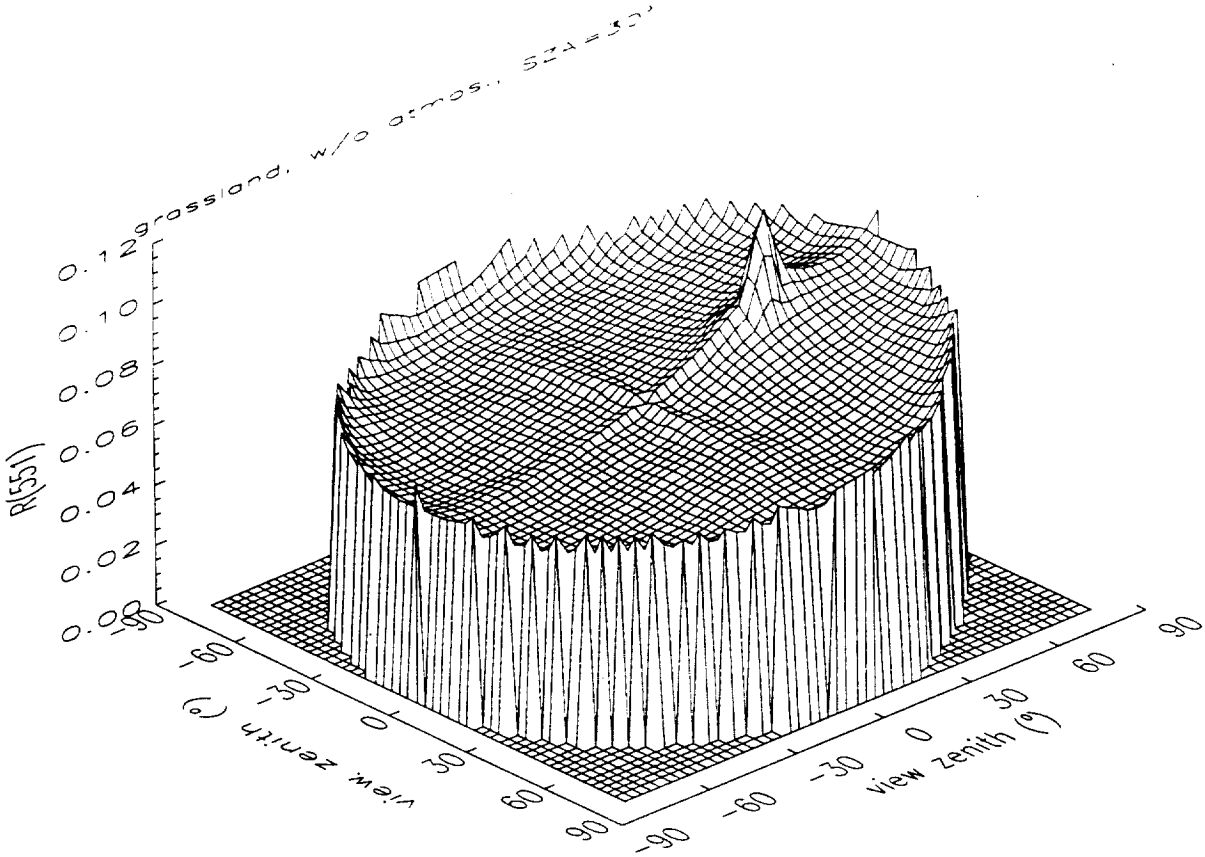
grassland, w/o atmos., SZA=30°
R(551)
0.12
0.10
0.08
0.06
0.04
0.02
0.00
-90
-60
-30
0
30
60
90
view zenith (°)
view zenith (°)

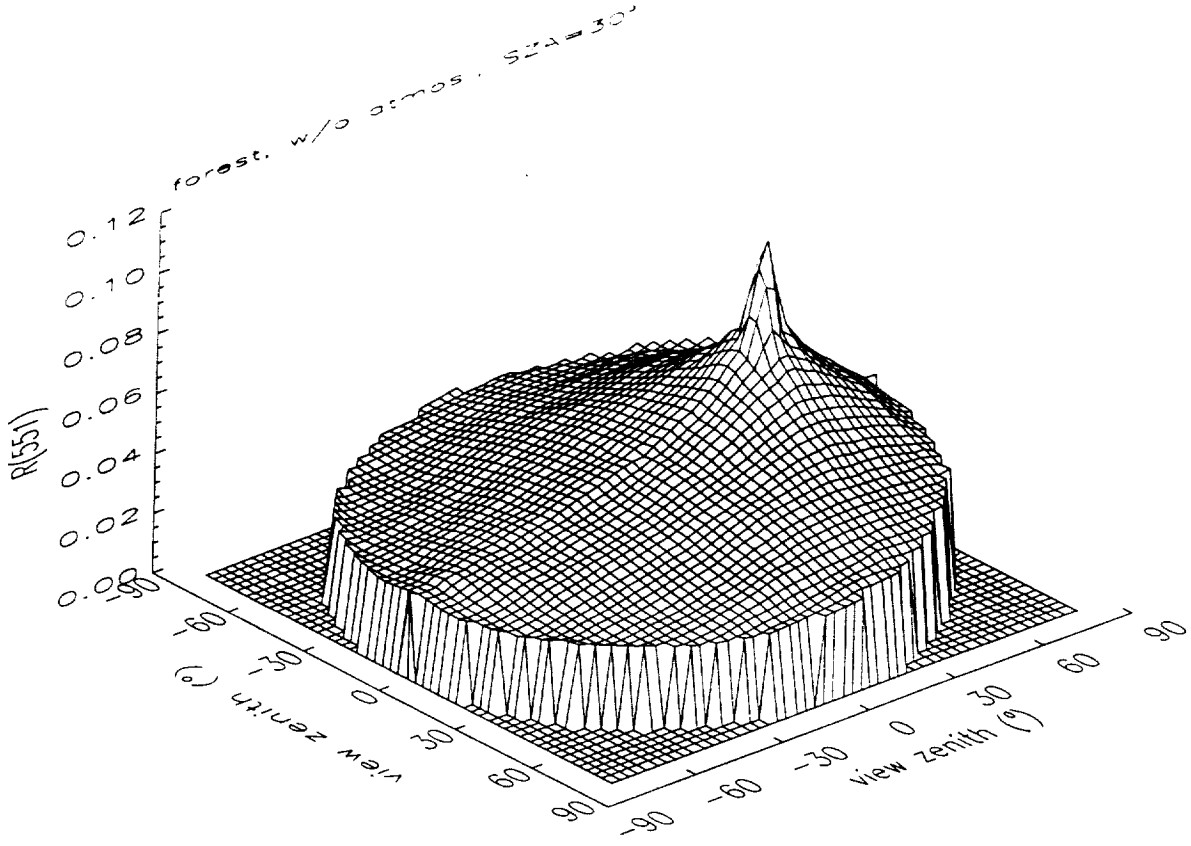
forest, w/o atmos, SZA=30°
R(551)
0.12
0.10
0.08
0.06
0.04
0.02
0.00
-90
-60
-30
0
30
60
90
view zenith (°)
-90
-60
-30
0
30
60
90
view zenith (°)

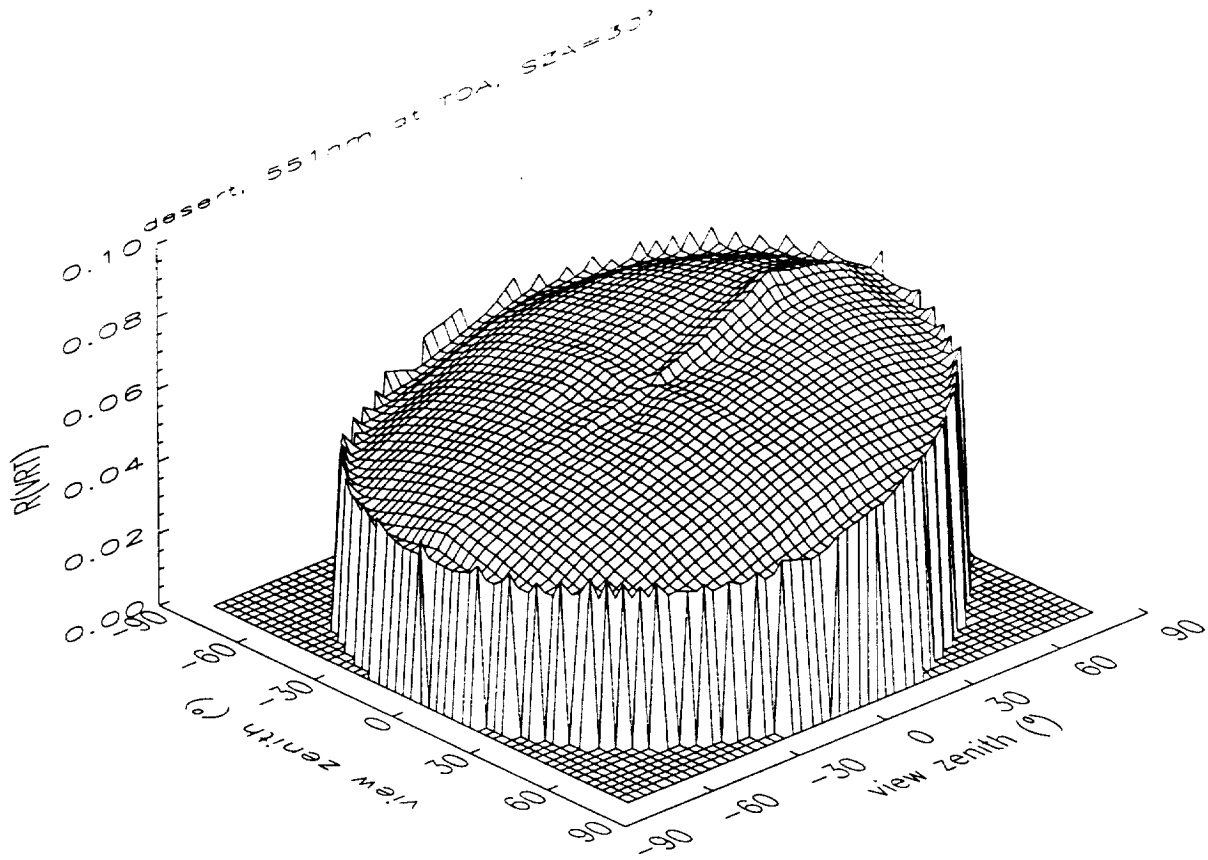
desert, 551nm at TOA, SZA=30°
R(VRT)
0.10
0.08
0.06
0.04
0.02
0.00
-90
-60
-30
0
30
60
90
view zenith (°)
-90
-60
-30
0
30
60
90
view zenith (°)

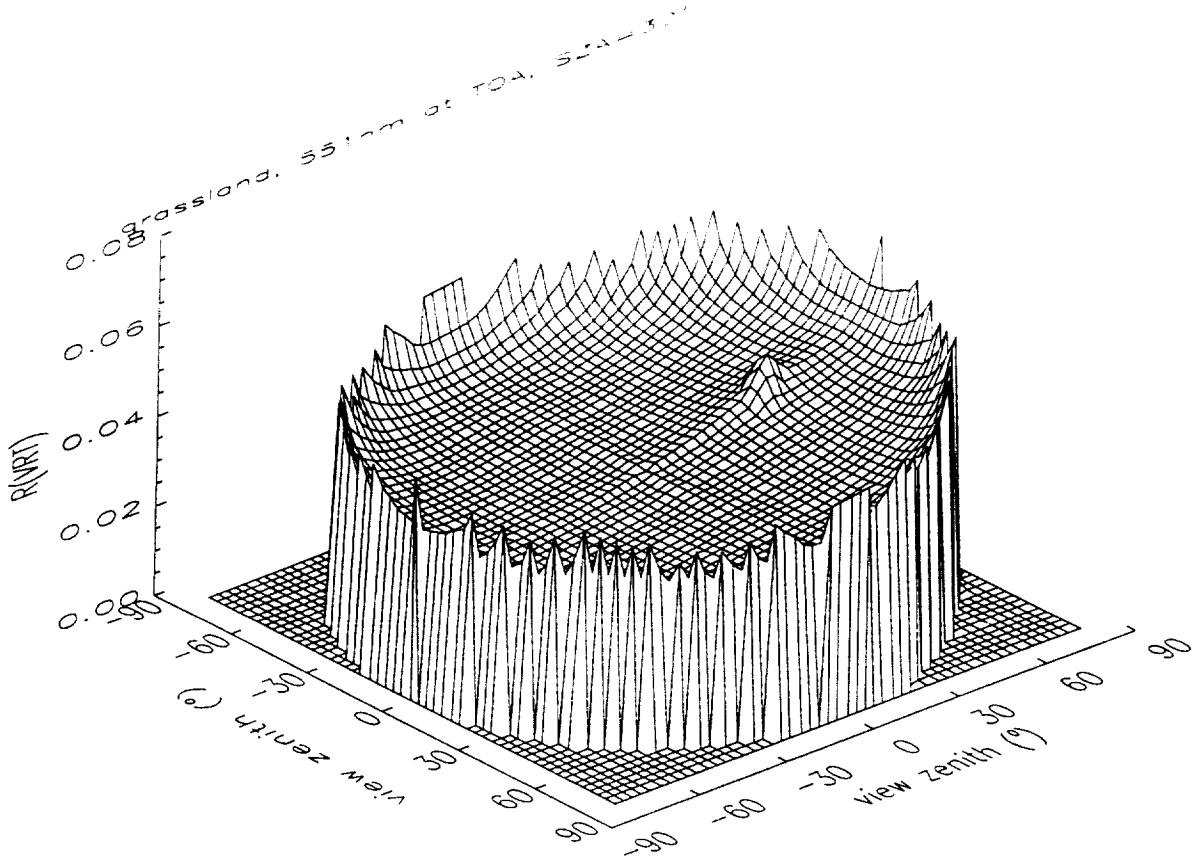
Grassland, 551nm at TOA, SZA=
R(VRF)
0.0
0.02
0.04
0.06
0.08
-90
-60
-30
0
30
60
90
view zenith (°)
-90
-60
-30
0
30
60
90
view zenith (°)

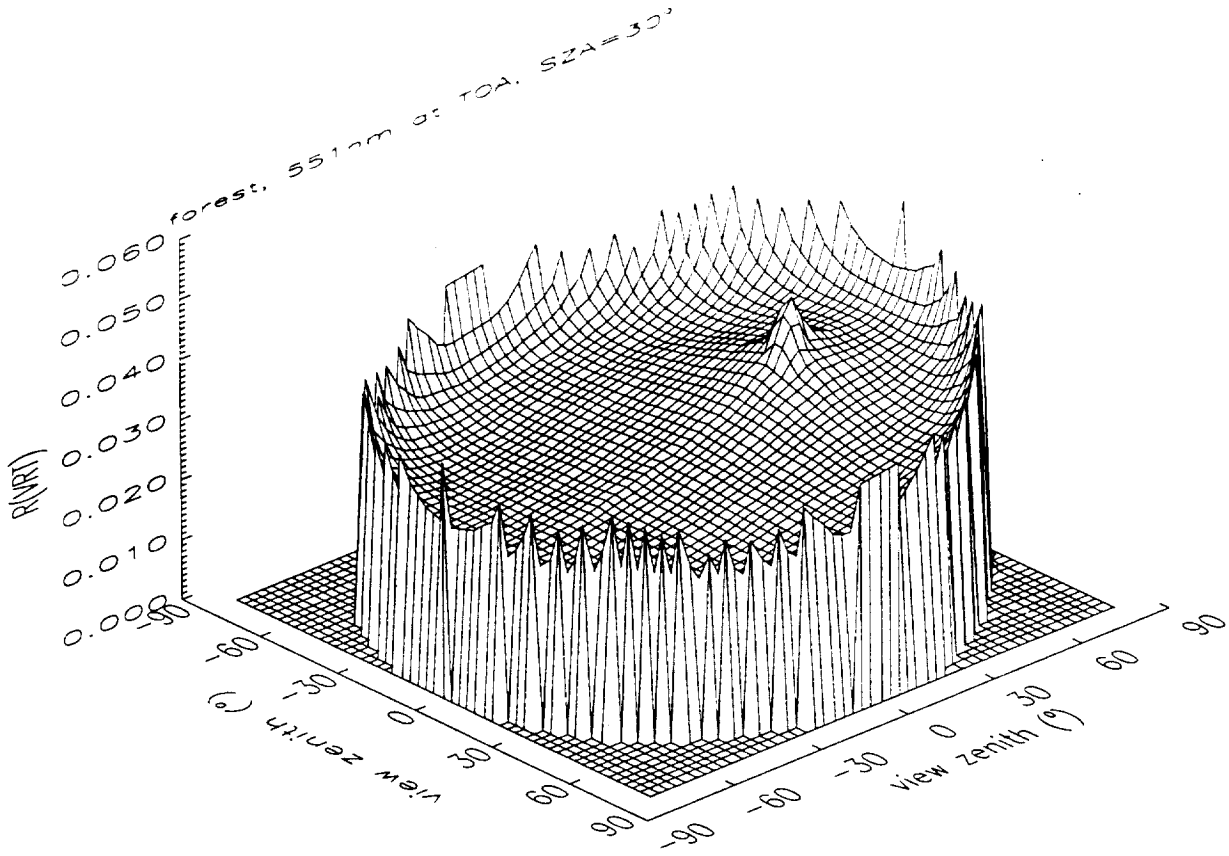
forest, 551nm at TOA, SZA=30°
R(VRT)
0.060
0.050
0.040
0.030
0.020
0.010
0.000
-90
-60
-30
0
30
60
90
view zenith (°)
view zenith (°)

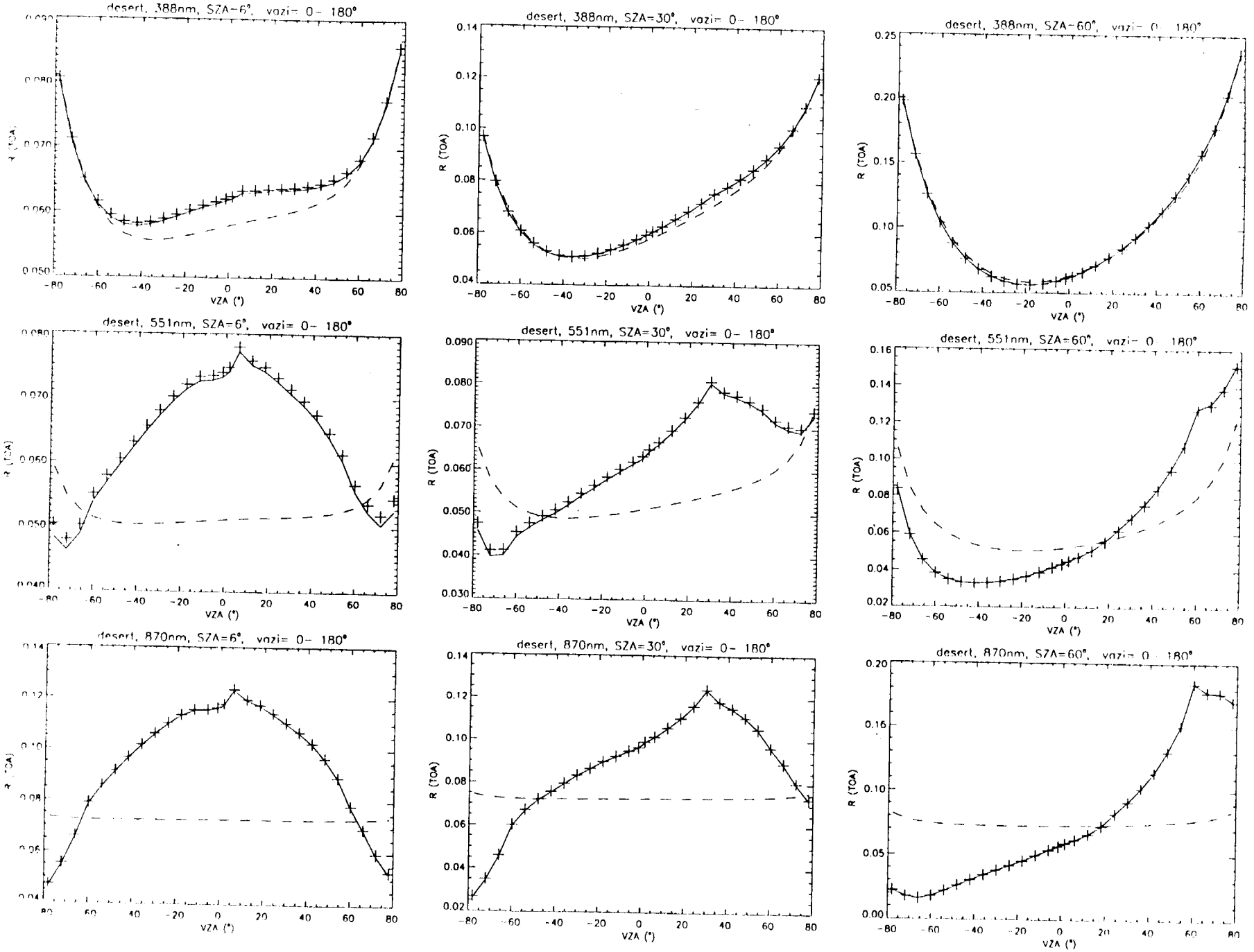
desert, 388nm, SZA=6°, vazi= 0- 180°
desert, 388nm, SZA=30°, vazi= 0- 180°
desert, 388nm, SZA=60°, vazi= 0- 180°
desert, 551nm, SZA=6°, vazi= 0- 180°
desert, 551nm, SZA=30°, vazi= 0- 180°
desert, 551nm, SZA=60°, vazi= 0- 180°
desert, 870nm, SZA=6°, vazi= 0- 180°
desert, 870nm, SZA=30°, vazi= 0- 180°
desert, 870nm, SZA=60°, vazi= 0- 180°
R (TOA)
VZA (°)

Fig 4

Fig 4

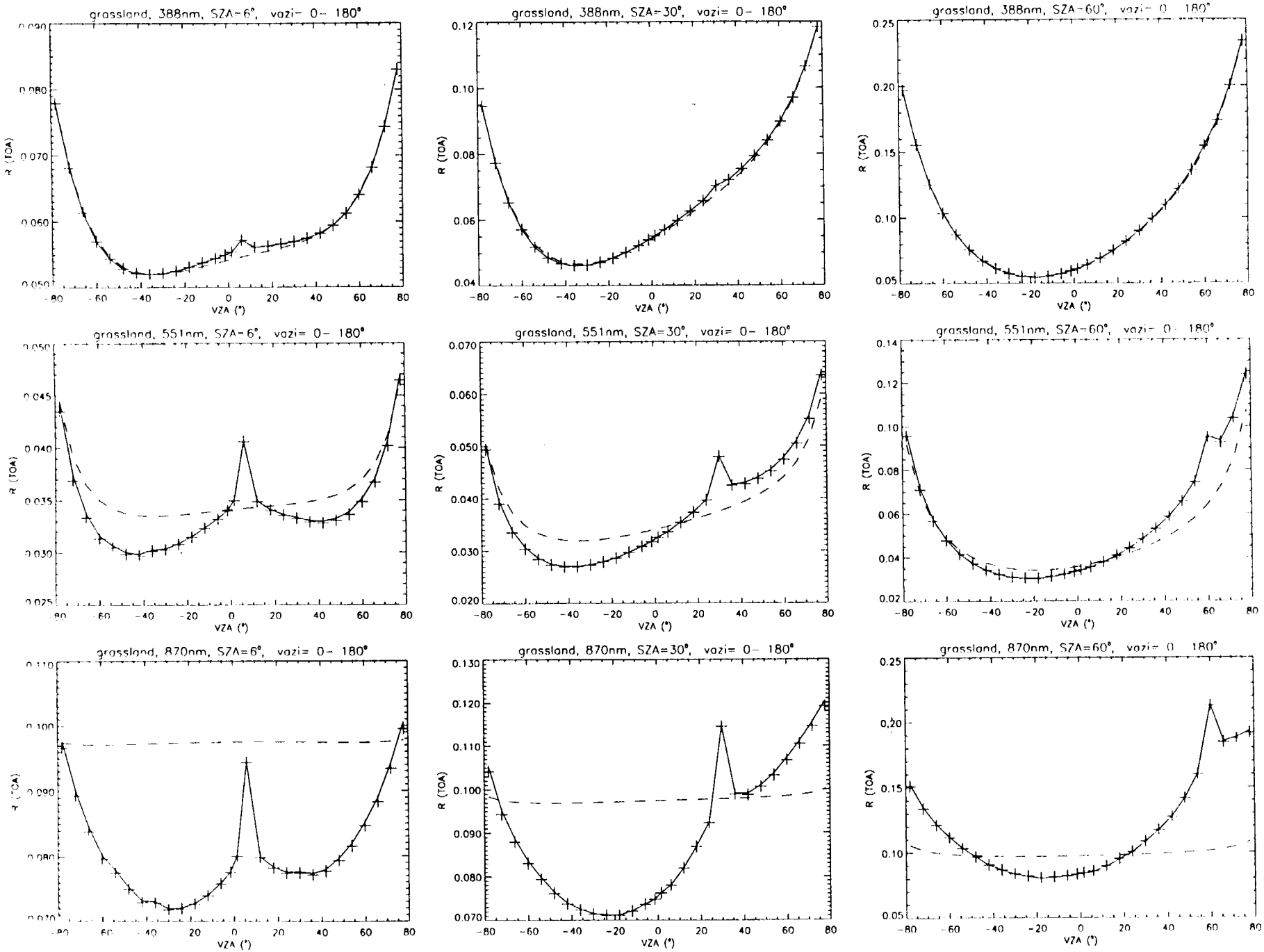
grassland, 388nm, SZA=6°, vazi= 0- 180°
grassland, 388nm, SZA=30°, vazi= 0- 180°
grassland, 388nm, SZA=60°, vazi= 0- 180°
grassland, 551nm, SZA=6°, vazi= 0- 180°
grassland, 551nm, SZA=30°, vazi= 0- 180°
grassland, 551nm, SZA=60°, vazi= 0- 180°
grassland, 870nm, SZA=6°, vazi= 0- 180°
grassland, 870nm, SZA=30°, vazi= 0- 180°
grassland, 870nm, SZA=60°, vazi= 0- 180°
R (TOA)
VZA (°)

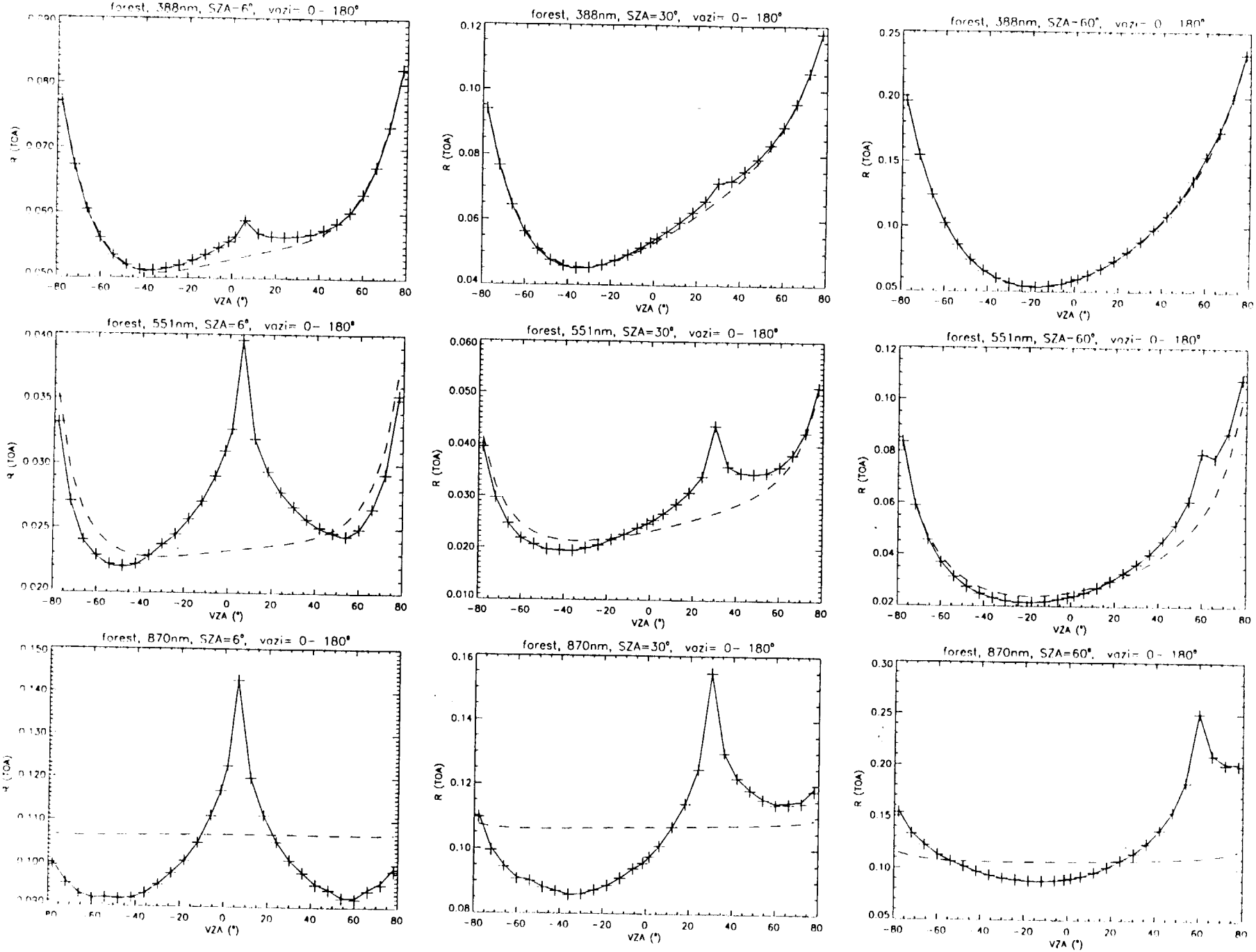
forest, 388nm, SZA=6°, vazi= 0- 180°
forest, 388nm, SZA=30°, vazi= 0- 180°
forest, 388nm, SZA=60°, vazi= 0- 180°
forest, 551nm, SZA=6°, vazi= 0- 180°
forest, 551nm, SZA=30°, vazi= 0- 180°
forest, 551nm, SZA=60°, vazi= 0- 180°
forest, 870nm, SZA=6°, vazi= 0- 180°
forest, 870nm, SZA=30°, vazi= 0- 180°
forest, 870nm, SZA=60°, vazi= 0- 180°
R (TOA)
VZA (°)

Fig. 6

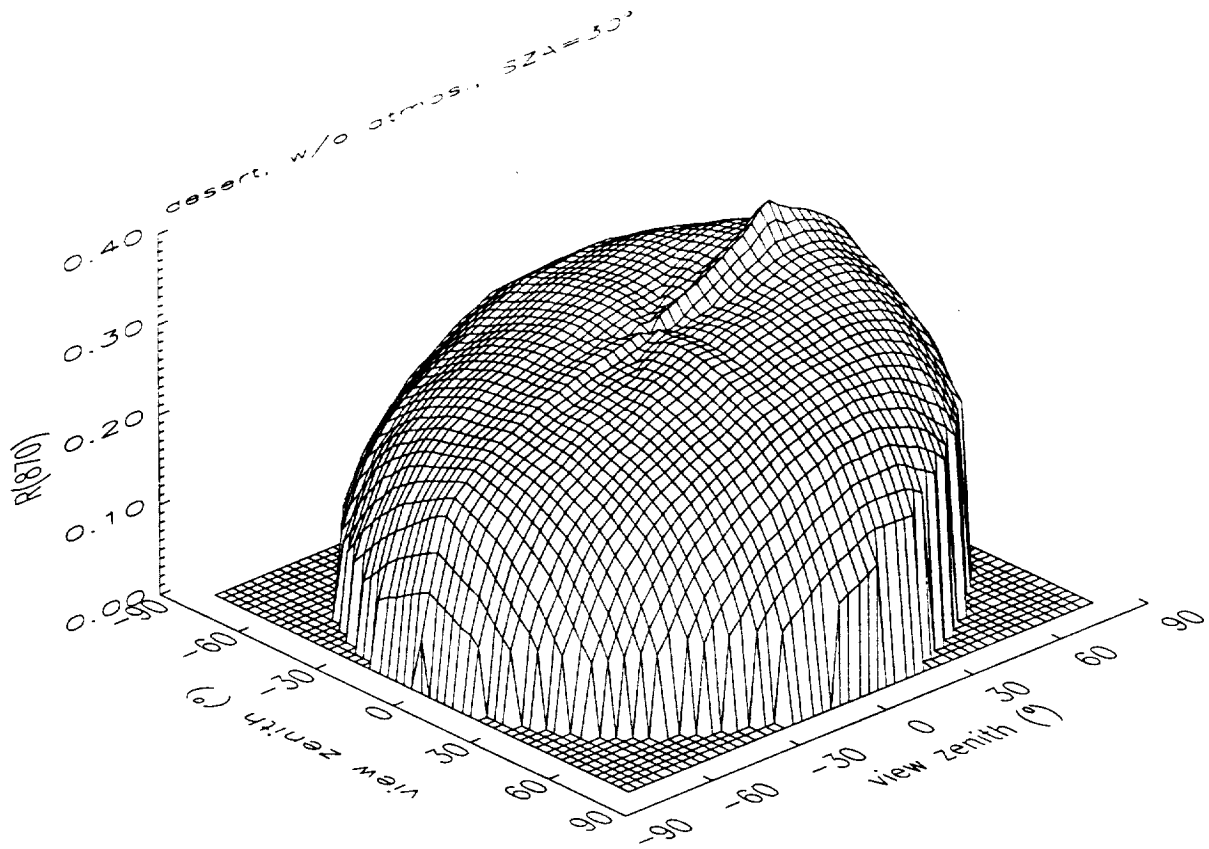
desert, w/o atmos., SZA=30°
R(870)
0.40
0.30
0.20
0.10
0.00
-90
-60
-30
0
30
60
90
view zenith (°)
-90
-60
-30
0
30
60
90
view zenith (°)

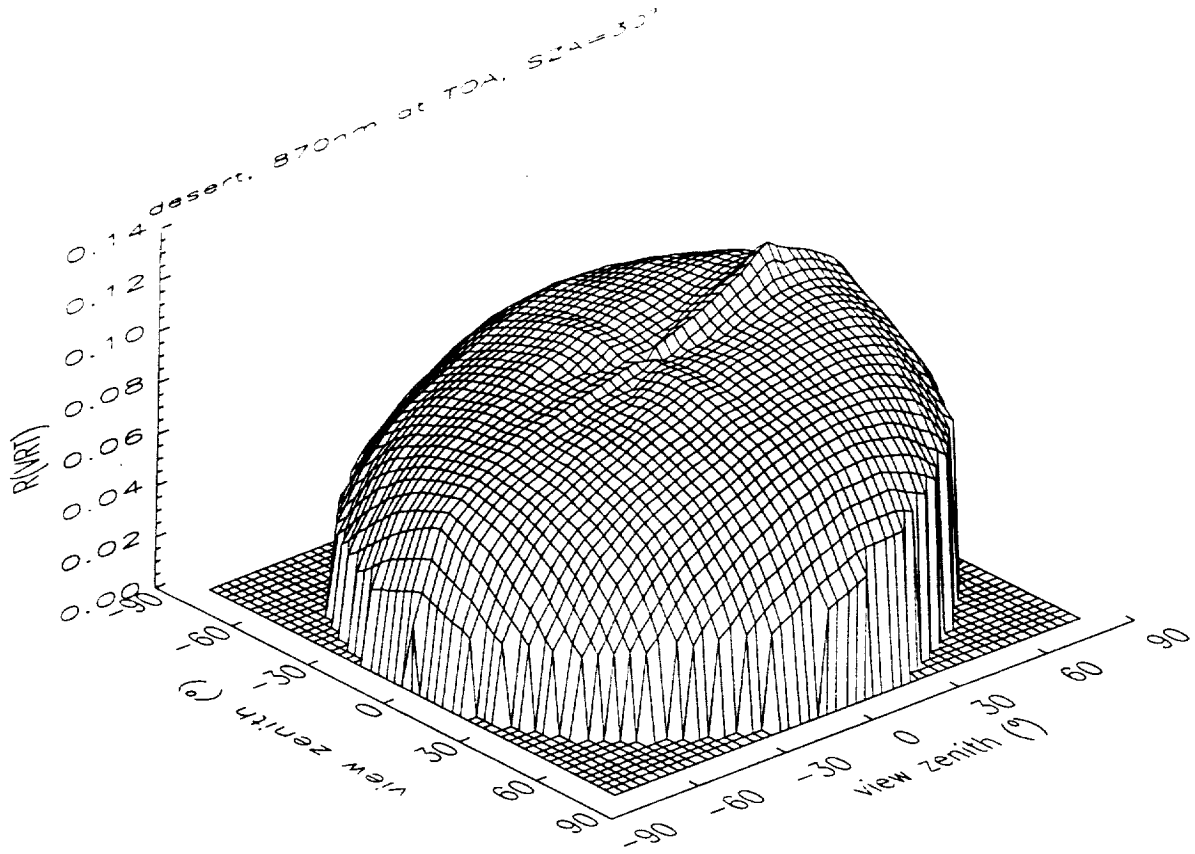
desert, 870nm at TOA, SZA=30°
R(VRT)
0.14
0.12
0.10
0.08
0.06
0.04
0.02
0.00
-90
-60
-30
0
30
60
90
view zenith (°)
-90
-60
-30
0
30
60
90
view zenith (°)

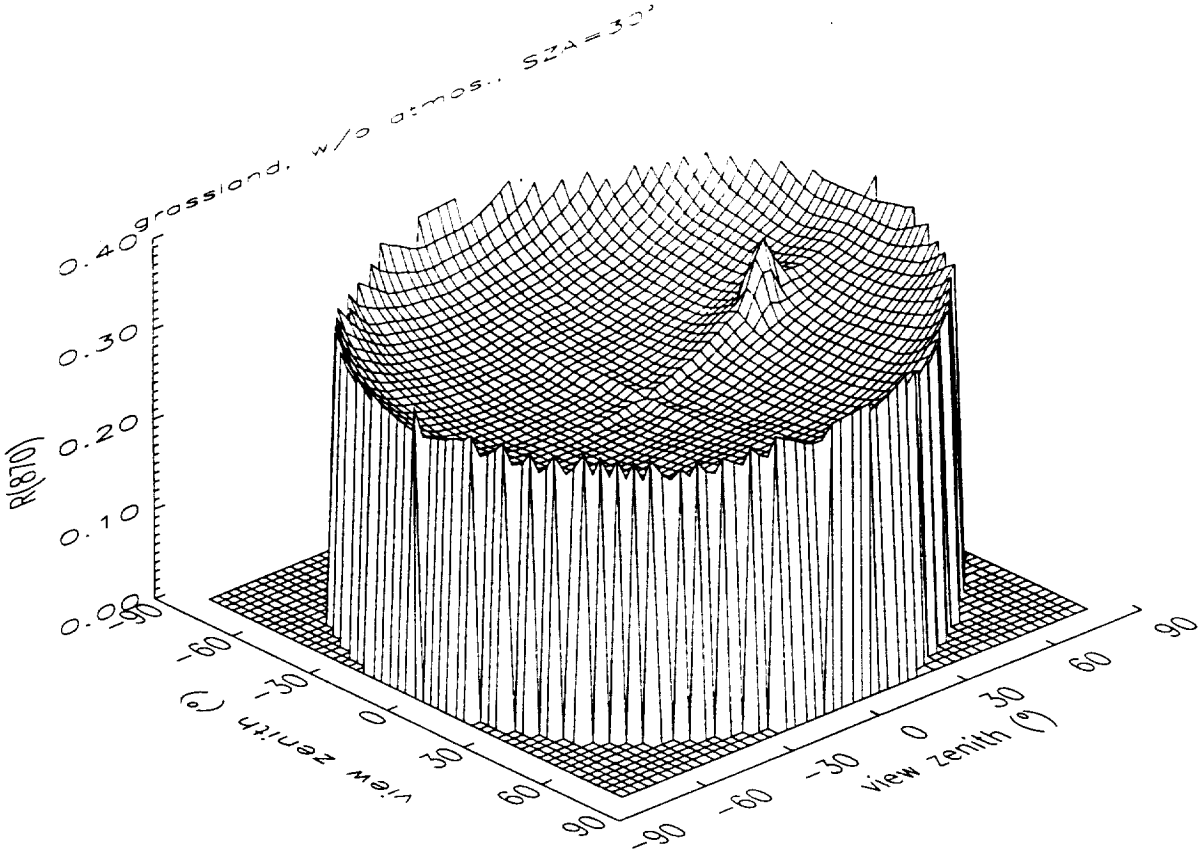
grassland, w/o atmos., SZA=30°
R(BTO)
0.40
0.30
0.20
0.10
0.00
-90
-60
-30
0
30
60
90
view zenith (°)
-90
-60
-30
0
30
60
90
view zenith (°)

Fig. 2. [illegible]

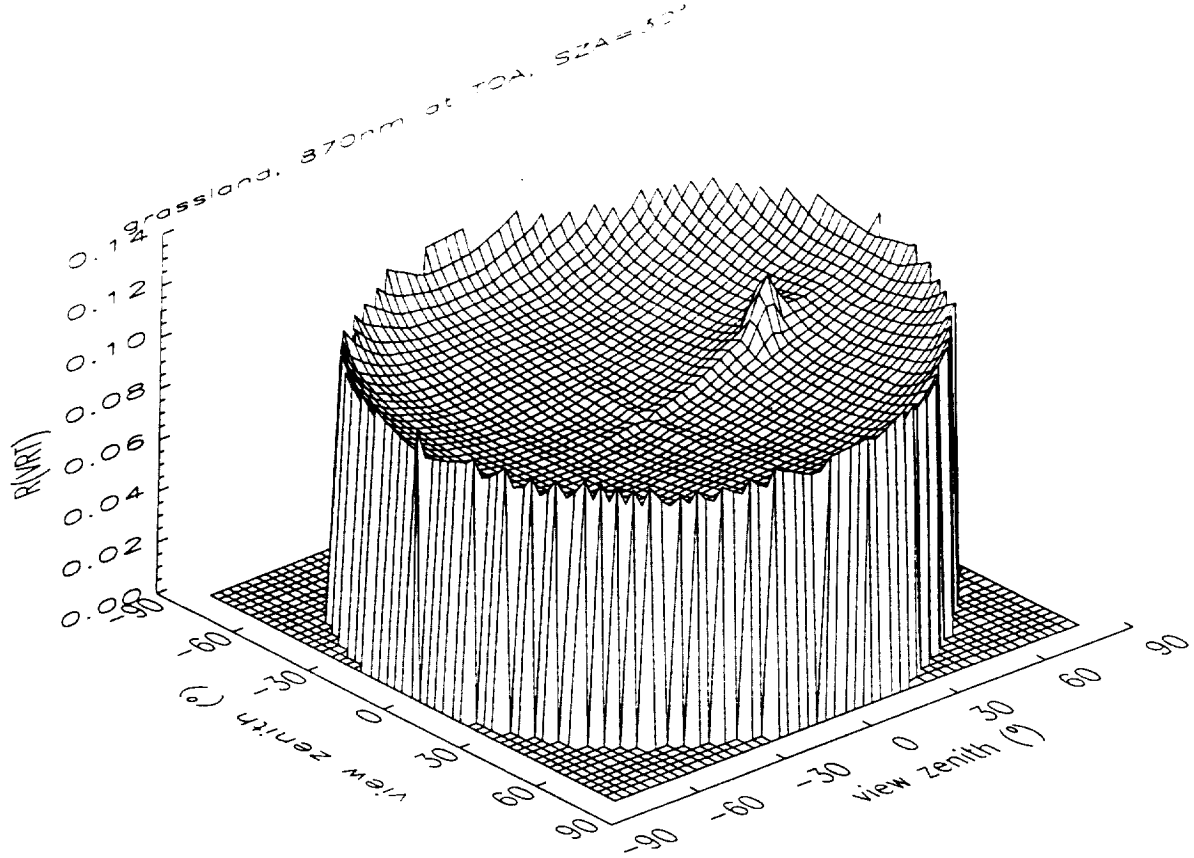
grassland, 870nm at TOA, SZA=
0.14
0.12
0.10
0.08
0.06
0.04
0.02
0.00
R(VRT)
-90
-60
-30
0
30
60
90
view zenith (°)
-90
-60
-30
0
30
60
90
view zenith (°)

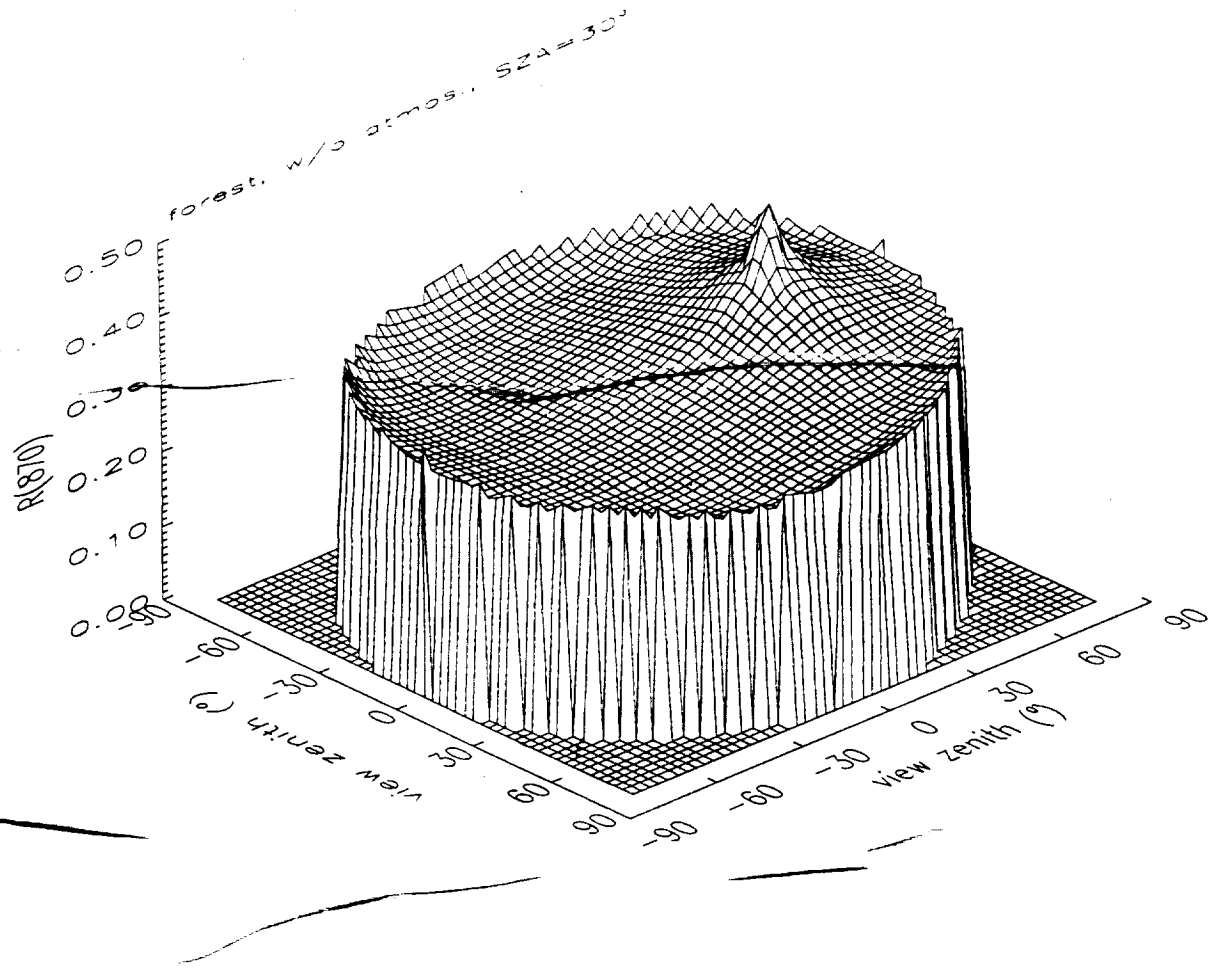
forest, w/o atmos., SZA=30°
R(870)
0.50
0.40
0.30
0.20
0.10
0.00
-90
-60
-30
0
30
60
90
view zenith (°)
-90
-60
-30
0
30
60
90
view zenith (°)

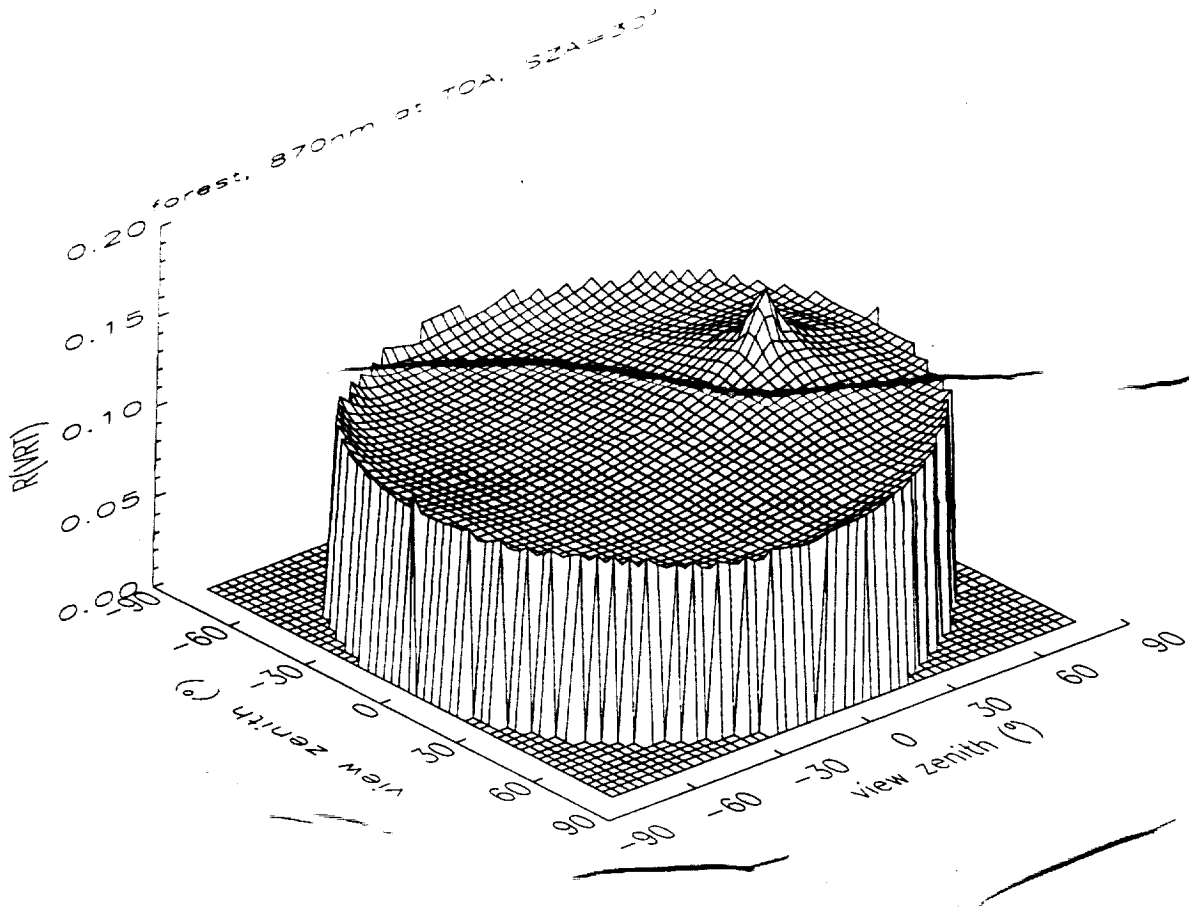
forest, 870nm at TOA, SZA=30°
R(VRT)
0.20
0.15
0.10
0.05
0.00
-90
-60
-30
0
30
60
90
view zenith (°)
-90
-60
-30
0
30
60
90
view zenith (°)